Biology of Reproduction, 2020, 103(3), 521–533
doi:10.1093/biolre/ioaa071
Research Article
Advance Access Publication Date: 15 May 2020

Research Article

Loss of myosin VI expression affects acrosome/acroplaxome complex morphology during mouse spermiogenesis†

Przemysław Zakrzewski[1], Maria Jolanta Rędowicz[2], Folma Buss[3] and Marta Lenartowska[1,4]

[1]Department of Cellular and Molecular Biology, Faculty of Biological and Veterinary Sciences, Nicolaus Copernicus University in Toruń, Torun, Poland, [2]Laboratory of Molecular Basis of Cell Motility, Nencki Institute of Experimental Biology, Polish Academy of Sciences, Warsaw, Poland, [3]Cambridge Institute for Medical Research, The Keith Peters Building, University of Cambridge, Cambridge, UK and [4]Centre for Modern Interdisciplinary Technologies, Nicolaus Copernicus University in Toruń, Torun, Poland

***Correspondence**: Department of Cellular and Molecular Biology, Faculty of Biological and Veterinary Sciences, Nicolaus Copernicus University in Toruń, Lwowska 1, 87-100 Torun, Poland. Tel: +48 56 611 31 86; E-mail: przezak@doktorant.umk.pl

†**Grant Support**: This project was supported by PRELUDIUM grant from the National Science Centre (Poland) to P.Z. (2017/25/N/NZ3/00487), an ETIUDA doctoral scholarship from the National Science Centre (Poland) to P.Z. (2018/28/T/NZ3/00002), a traveling fellowship for P.Z. funded by The Company of Biologists (JCSTF-171105) and a Medical Research Council program grant to F.B. (MR/S007776/1).
Conference Presentation: Presented in part at the 43rd FEBS Congress, 7–12 July 2018, Prague, Czech Republic, and the 44th FEBS Congress, 6–11 July 2019, Krakow, Poland.
F.B. and M.L. contributed equally to this work and are joint senior authors.

Received 2 February 2020; Revised 24 March 2020; Accepted 14 May 2020

Abstract

During spermiogenesis in mammals, actin filaments and a variety of actin-binding proteins are involved in the formation and function of highly specialized testis-specific structures. Actin-based motor proteins, such as myosin Va and VIIa, play a key role in this complex process of spermatid transformation into mature sperm. We have previously demonstrated that myosin VI (MYO6) is also expressed in mouse testes. It is present in actin-rich structures important for spermatid development, including one of the earliest events in spermiogenesis—acrosome formation. Here, we demonstrate using immunofluorescence, cytochemical, and ultrastructural approaches that MYO6 is involved in maintaining the structural integrity of these specialized actin-rich structures during acrosome biogenesis in mouse. We show that MYO6 together with its binding partner TOM1/L2 is present at/around the spermatid Golgi complex and the nascent acrosome. Depletion of MYO6 in Snell's waltzer mice causes structural disruptions of the Golgi complex and affects the acrosomal granule positioning within the developing acrosome. In summary, our results suggest that MYO6 plays an anchoring role during the acrosome biogenesis mainly by tethering of different cargo/membranes to highly specialized actin-related structures.

Summary Sentence

Myosin VI is required for the maintenance of correct morphology of testis-specific actin-containing structures important for acrosome development in mouse such as the Golgi complex and the acrosome–acroplaxome complex.

Key words: acrosome/cap, acroplaxome, actin cytoskeleton, Golgi complex, myosin VI, Snell's waltzer mice.

Introduction

Actin filaments are ubiquitously present in eukaryotic cells and play a fundamental role in cell differentiation and function. The actin cytoskeleton together with actin-binding proteins (ABPs) provides both structural support and functional flexibility, performing key roles in many cellular processes including cell motility, intracellular trafficking, and cell division. In addition, microfilaments form cell type-specific cytoskeletal arrays that are crucial for the subcellular organization, asymmetric positioning of specialized compartments, maintenance of cell shape, and formation of highly specialized cell structures. The actin cytoskeleton is also crucial for a number of cellular processes during spermatogenesis and is thus essential for male fertility [1].

Spermiogenesis, the last step of sperm development, is a complex transformation process of unpolarized spermatids into morphologically mature spermatozoa. In mammals this process is typically divided into three successive steps: the Golgi phase, acrosome/cap phase, and maturation phase. One of the earliest events during spermiogenesis is acrosome formation, an apical nuclear cap rich in hydrolytic enzymes, which is required for sperm penetration of the oocyte at fertilization. Biogenesis of the acrosome begins with trafficking of proacrosomal vesicles toward the spermatid nucleus from both the *trans*-Golgi network and the endocytic pathway [2]. These vesicles adhere to and fuse to form the acrosomal vesicle along the acroplaxome, a cytoskeletal actin-rich plate that anchors the developing acrosome to the nuclear envelope [3]. The large acrosomal vesicle then progressively spreads over the spermatid nucleus to form a distinct cap-like structure. As spermiogenesis proceeds, a transient cytoskeletal structure, the manchette, develops to exert mechanical force for nuclear compaction/elongation and to serve as a scaffold for transport of molecules to the growing flagellum. The acroplaxome also expands during maturation phase, thus potentially supporting the manchette complex in nuclear shaping [4]. Two additional testis-specific structures are formed to support spermiogenesis efficiently: (i) apical ectoplasmic specialization that anchors the developing spermatid to the Sertoli cell during its movement in the seminiferous tubules and (ii) tubulobulbar complexes at the Sertoli–spermatid interface [5, 6]. Finally, excess cytoplasm (the residual body) is removed from the maturing spermatid and phagocytozed by the Sertoli "nurse" cell.

It has been long recognized that the actin cytoskeleton together with various ABPs participates in assembly and remodeling of these unique, testis-specific structures including the acrosome–acroplaxome complex [1]. The experimental disruption of actin filaments results in detachment of the acrosome from the spermatid nucleus and deformation of the expanding edge of the acrosomal sac, suggesting that the correct actin assembly is crucial for acrosomogenesis [7]. A number of actin regulators, such as cortactin and profilin, are present in the acrosome–acroplaxome-manchette complex and thus may regulate actin dynamics during the acrosome biogenesis and the head shaping [8, 9]. Furthermore, actin-based motors such as myosin Va and VIIa are components of the acroplaxome and are associated with vesicles in the manchette during acrosome biogenesis and sperm flagellum development [10, 11].

In addition to myosin Va and VIIa, myosin VI (MYO6) is also expressed in mouse testes, where it is present in actin-rich structures during acrosome biogenesis such as the Golgi complex and the acrosome-acroplaxome complex [[12]; summarized in Figure 1]. MYO6 is expressed in most cell types and tissues, and since it is the only pointed-end-directed actin-based motor, it participates in several cellular processes including endocytosis, Golgi organization and function, basolateral targeting and sorting in the secretory pathway, epithelial integrity, and cell adhesion and migration [13–15]. Similar to vertebrates, loss of MYO6 in *Drosophila* is not lethal, but causes a variety of well-documented phenotypes during embryogenesis and development [16–18], including severe abnormalities during *Drosophila* spermiogenesis (called spermatid individualization) leading to male sterility [19, 20]. Mutation in the *Myo6* gene in Snell's waltzer mice (*sv/sv*) causes deafness as a result of neurosensory epithelia degeneration in the inner ear [21]. Moreover, the *sv/sv* mice display several other defects such as changes in Golgi morphology, reduced secretion, and defective endocytosis and autophagy [22–25]. Moreover, data from our lab shows that male *sv/sv* mice have significantly reduced fertility and exhibit disruption of the spatial organization of the apical tubulobulbar complexes during the late stage of spermiogenesis [26]. Here, we show, by comparing the morphology of developing spermatids of control and MYO6-deficient male mice, that this myosin is present in actin-rich structures during acrosome biogenesis and supports the integrity of these testis-specific structures at this stage of mouse sperm development.

Materials and methods

Ethics statement

All animal work was performed at the Nencki Institute of Experimental Biology (Warsaw, Poland) or at the University of Cambridge, Cambridge Institute for Medical Research in accordance with the UK Animals (Scientific Procedures) Act of 1986 (PPL70/8460). The mice were bred and housed under pathogen-free conditions. Animal were housed and euthanized in compliance with the European Communities Council directives adopted by the Polish Parliament (Act of 15 January 2015 on the use of animals in scientific investigations) and with the UK Animals (Scientific Procedures) Act 1986 and Laboratory Animal Science Association (LASA) guidelines.

Animals

Three-month-old male Snell's waltzer mice (*sv/sv*, C57BL/6 background) were used in the study. A spontaneously mutated *sv* allele encodes *Myo6* gene with a 130-bp deletion resulting in the introduction of a stop codon in the neck region of MYO6 [21]. No MYO6 is detected in any tissue of homozygous *sv/sv* mice, including testis (Figure 2A). Each experiment was performed at least three

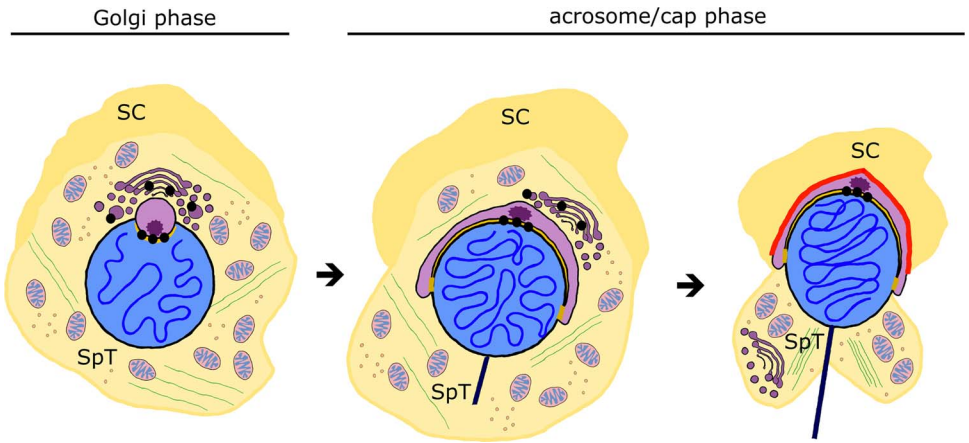

Figure 1. Schematic representation of the acrosome biogenesis and the localization of MYO6 during this process in mouse. Black dots, MYO6; SC, Sertoli cell; SpT, spermatid; red line, apical ectoplasmic specialization and yellow line, acroplaxome.

times using a pair of control (heterozygous, *sv*/+) and mutant (*sv*/*sv*) males from one litter. Importantly, heterozygous mice express approximately equal amount of MYO6 in comparison with wild-type mice [22].

Antibodies and reagents

For the primary antibodies used in this study, please see supplementary Table S1. The secondary antibodies used for immunofluorescence were goat anti-rabbit/mouse Alexa Fluor 488/568 (Invitrogen). For immunogold labeling, Protein A gold conjugates (Department of Cell Biology, University of Utrecht, the Netherlands) were used to detect primary antibodies. The secondary anti-mouse/rabbit antibodies used for immunoblotting were horseradish peroxidase (HRP) conjugated (Sigma). F-actin was visualized using Alexa Fluor 488 Phalloidin (Invitrogen). Nuclei were counterstained with Hoechst 33342 (Thermo Scientific). Acrosomes were stained either with Coomassie Brilliant Blue (Sigma-Aldrich) or lectin PNA from peanut Alexa Fluor 488 conjugate (Invitrogen). Normal rabbit IgG (Sigma-Aldrich) was used as a negative control during immunofluorescence and immunogold experiments [26].

Immunoblotting

Testes dissected from *sv*/+ and *sv*/*sv* males (n = 3 for both mutant and control males) were homogenized with a Dounce tissue grinder in protein extraction buffer (50 mM Tris-HCl pH 7.5, 0.5% Triton X-100, 150 mM NaCl, 5% glycerol) supplemented with 1 × cOmplete Protease Inhibitor Cocktail (Roche). The homogenates were centrifuged twice at 15 000 × g for 10 min at 4 °C, and protein concentration of the supernatants was determined using the Bio-Rad DC Protein Assay according to the manufacturer's instructions. Equal amounts of protein extract were separated by electrophoresis on a 7% SDS-PAGE gels, and then transferred to Amersham PVDF Hybond P membrane (GE Healthcare). Blocked blots were probed with the primary antibodies overnight at 4 °C, washed, and incubated for 1 h with the corresponding anti-rabbit secondary IgG antibody conjugated with HRP. Signals were detected with the Amersham ECL Advance Western Blotting Detection Kit according to the manufacturer's guidelines (GE Healthcare). All immunoblotting experiments were repeated three times.

Conventional electron microscopy

For detailed ultrastructural analysis, dissected testes were immersion fixed in 2% (v/v) glutaraldehyde in 0.1 M cacodylate buffer (pH 7.4) for 2 h at room temperature. Tunicae albugineae of the testes were punctured with a syringe needle to facilitate fixative penetration. Pre-fixed samples were then cut into small pieces and further fixed overnight at 4 °C. Next, the samples were post-fixed with 1% (v/v) osmium tetroxide in cacodylate buffer for 1 h at 4 °C, dehydrated in ethanol, and embedded in Spurr resin (Sigma-Aldrich) according to the standard protocol. Ultrathin sections (cross-sections of seminiferous tubules) were collected on copper grids, post-stained with 2.5% uranyl acetate and 0.4% lead citrate solutions, and examined and imaged on a JEM 1400 transmission electron microscope (JEOL Co.) equipped with 11 Megapixel TEM Morada G2 digital camera (EMSIS GmbH) or an FEI Tecnai G2 Spirit BioTwin transmission electron microscope equipped with a Gatan CCD camera. Acquired images were processed using Adobe Photoshop CS6. Ultrastructural images are representative from experiments repeated at least three times.

Sample preparation for immunocytochemical studies

Epithelial fragments for immunofluorescence were prepared as follows: the dissected testes from *sv*/+ and *sv*/*sv* males were decapsulated and minced in 4% formaldehyde in 1 × PBS (pH 7.4) and fixed overnight at 4 °C. The fixed seminiferous tubules segments were aspirated gently through 18-gauge and 21-gauge syringe needles [27]. Larger fragments of tissue were allowed to settle to the bottom of the tube, before the supernatant was removed and centrifuged (1 min at 4000 × g). The pellet was resuspended in PBS, and the cell suspension was added onto poly-L-lysine-coated coverslips. After 10 min, the coverslips were plunged into ice-cold acetone and air dried.

Immunolocalization studies

For immunofluorescence studies, samples were blocked with 1% BSA/0.1% Triton X-100 before incubating with primary antibodies overnight at 4 °C, which were detected with secondary antibodies conjugated with different fluorochromes. DNA was stained with Hoechst. Epi-fluorescence images were captured on Zeiss Axio

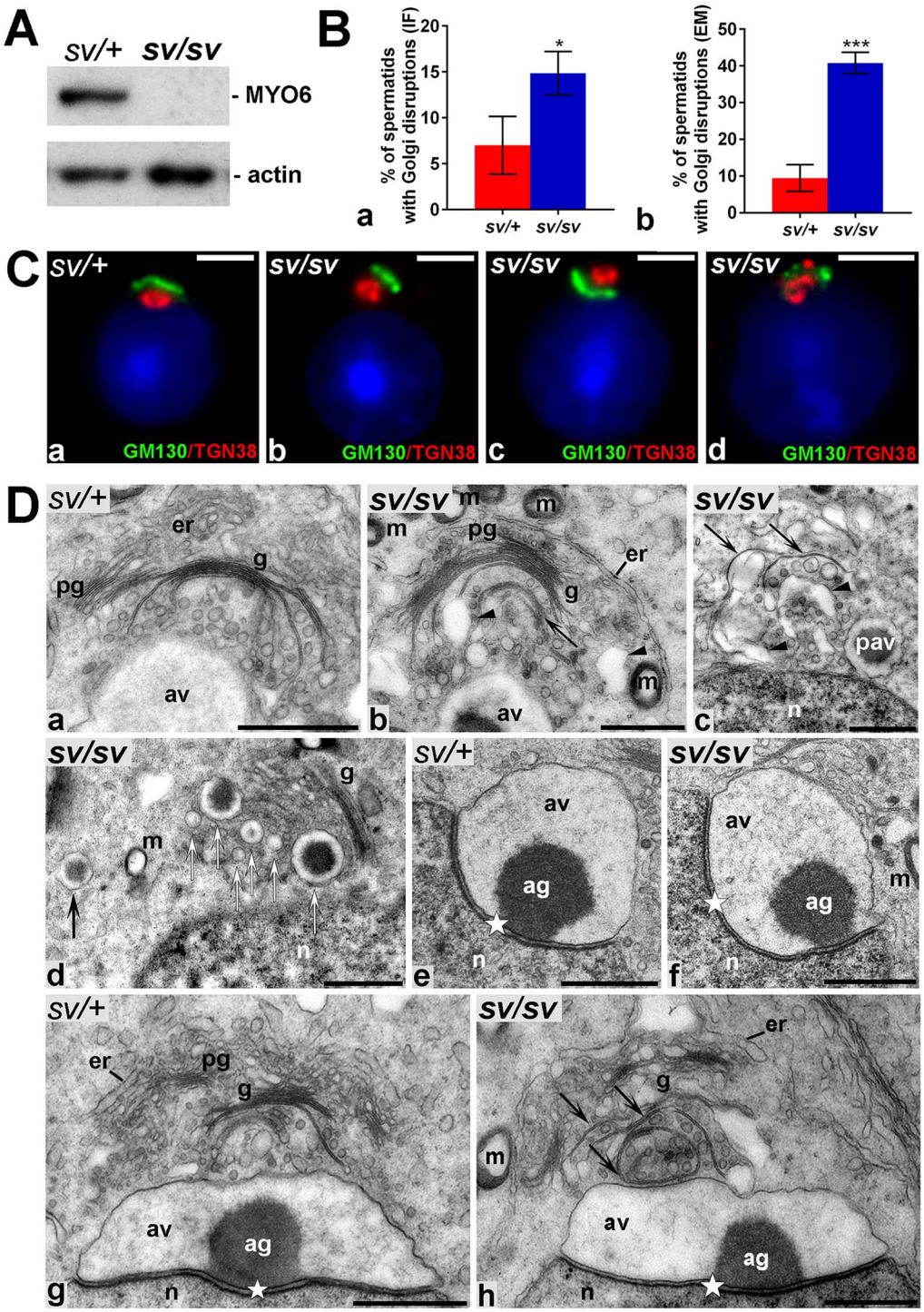

Figure 2. The acrosomogenesis in MYO6-deficient spermatids is altered. (A) Immunoblotting of crude protein extracts from *sv/+* and *sv/sv* testes with anti-MYO6 and anti-actin antibodies. No MYO6 is detectable in *sv/sv* tissue. (B) The graphs depicting the mean percentage of *sv/+* and *sv/sv* cells that displayed the Golgi defects visualized with a use of immunofluorescence (IF) (a) and ultrastructural (EM) (b) analysis. For immunofluorescence, counts were performed on >90 cells from $n = 3$ independent experiments. For ultrastructure analysis, counts were performed on at least four ultrathin sections of seminiferous tubules from randomly chosen fragments of fixed testes from $n = 3$ independent experiments.. Error bars indicate SD. $^{*}P \leq 0.05$; $^{***}P < 0.001$. (C) Immunofluorescence localization of TGN38 (red) and GM130 (green) in *sv/+* and *sv/sv* round spermatids. Bars 2 µm. (D) Ultrastructural analysis of *sv/+* and *sv/sv* spermatids during the consecutive phases of acrosomogenesis. ag, acrosomal granule; av, acrosomal vesicle; er, endoplasmic reticulum; g, Golgi complex; m, mitochondria; n, nucleus; pav, proacrosomal vesicle; pg, proximal Golgi; and white star, acroplaxome. All other indications are explained in the text. Bars 1 µm.

Imager.Z2 upright microscope and the acquired images were processed with Zeiss ZEN 2.6 (blue edition) and Adobe Photoshop CS6 software.

For post-embedding immunogold labeling for electron microscopy, samples were fixed with 4% formaldehyde and 0.25% glutaraldehyde in 1 × PBS (pH 7.4), dehydrated in ethanol, before embedding in LR Gold resin (Sigma-Aldrich) according to the standard protocol. Samples in resin were cut with a diamond knife into ultrathin sections, collected onto nickel grids, and blocked 5 min at room temperature with 1% BSA in PBS (pH 7.4). The sections were then incubated overnight with primary antibody in 0.1% BSA/PBS at 4 °C and the next day with 10 nm gold-conjugated protein A (at dilution 1:50 in 0.1% BSA/PBS) for 60 min at room temperature. Finally, the sections were post-fixed with 1% glutaraldehyde in PBS, post-stained with 2.5% uranyl acetate and 0.4% lead citrate solutions, and examined and imaged on an FEI Tecnai G2 Spirit BioTwin transmission electron microscope equipped with a Gatan CCD Camera. Acquired images were processed with Adobe Photoshop CS6. Representative images for immunolocalization studies were collected from experiments repeated at least three times.

Epididymal sperm count and acrosomal reaction

Caudae epididymides from *sv*/+ and *sv*/*sv* males were dissected, cut in several places with a sharp scalpel blade, and incubated for 15 min in Whittens-HEPES medium (100 mM NaCl, 4.4 mM KCl, 1.2 mM KH_2PO_4, 1.2 mM $MgSO_4$, 5.4 mM glucose, 0.8 mM pyruvic acid, 4.8 mM lactic acid, and 20 mM HEPES) at 37 °C to allow the sperm to swim out from the incisions. A proportion of the collected sperm was diluted 1:10 with distilled water and transferred to a hemocytometer for sperm counting. Another fraction of the sperm was diluted 1:1 with a 2 × capacitation media (Whittens-HEPES medium supplemented with 30 mM $NaHCO_3$ and 10 mg/ml BSA) and incubated for 60 min at 37 °C. After the capacitation, the acrosomal reaction was induced by incubation for 30 min in 10 µM A23187 ionophore (Sigma-Aldrich). Both capacitated and acrosome-reacted sperm were fixed with 5% formaldehyde in PBS (pH 7.4) for 10 min in room temperature, washed, smeared on glass slides, and air dried. Acrosomes were visualized by immersion of slides in Coomassie Brilliant Blue staining solution (Coomassie dye in 50% methanol and 10% acetic acid). For sperm head and acrosome structure analysis, epididymal sperm were stained with Hoechst and lectin PNA Alexa Fluor 488 conjugate (1:100 dilution in 1 × PBS) for 10 min at room temperature. Representative images were collected from experiments repeated at least three times.

Statistical analysis

The obtained results were presented as the mean ± SD. The statistical significance in each experiment was analyzed using an unpaired two-tailed Student *t*-tests. The data were considered significant when $P < 0.05$. All data analysis was performed using GraphPad Prism 6 for Windows.

Results

In this study, we focus on the comparative analysis of acrosome biogenesis during the Golgi and the acrosome/cap phases (Figure 1) in MYO6-deficient and control mice using cyto/immunocytochemistry and epi-fluorescence microscopy as well as electron microscopy for ultrastructural studies. Our results show that MYO6 deficiency in mouse testes leads to structural defects in developing spermatids affecting correct acrosome formation.

MYO6 depletion causes structural disruptions during early acrosome biogenesis

Our previous results have shown that in wild-type mice, MYO6 is present at actin-rich structures involved in acrosome formation, such as the Golgi complex and the acrosome–acroplaxome complex (Figure 1) [12]. We therefore analyzed here whether this motor protein has a role in acrosomogenesis by testing whether MYO6 is important for maintaining the morphology of the testis-specific structures during acrosome biogenesis. We used testes dissected from *sv*/*sv* mice, which do not express any MYO6 (Figure 2A), and compared organization of the Golgi complex in *sv*/*sv* and control spermatids (Figure 2C). Developing spermatids at the Golgi stage were labeled with antibodies to GM130 (a marker for the *cis*-Golgi) and to TGN38 (specific for the *trans*-Golgi). As shown in Figure 2C.a, the functional sub-domains of the Golgi complex are correctly oriented and stacked relative to spermatid nuclei in *sv*/+ spermatids; the staining for *cis*-Golgi corresponded to the semi-circular shape of the organelle observed at the ultrastructural level (compare Figure 2C.a and D.a). In contrast, in *sv*/*sv* spermatids, the mislocalization of these Golgi markers suggests a partial disorganization of the Golgi complex that in some cases was asymmetrically oriented (Figure 2C.b) or completely inverted (Figure 2C.c). In most extreme examples, we could observe a severe loss of Golgi morphology and no segregation between the *cis*-Golgi and *trans*-Golgi sub-domains (Figure 2C.d). Finally, quantification and statistical analysis of these phenotypes revealed that in control mice 7.00 ± 3.15% of spermatids exhibited Golgi structural defects compared to 14.86 ± 2.37% observed in *sv*/*sv* mice, indicating a two-fold increase of Golgi disorganization in mutant spermatids (Figure 2B.a; $P = 0.026$; $n = 3$ individual experiments on a pair of *sv*/+ and *sv*/*sv* littermates each).

Next, we examined in detail the ultrastructure of spermatids during acrosomogenesis in *sv*/*sv* and control testes. At the beginning of acrosome biogenesis, we observed in control spermatids a Golgi complex that is located near the spermatid nucleus and forms a semi-circular structure with its concave *trans*-side rich in vesicles, facing the nucleus (Figure 2D.a). In control testes, the Golgi stacks have tightly aligned flattened cisternae and no separation between the individual cisternae. In *sv*/*sv* spermatids, however, the Golgi cisternae did not form regular stacks but were separated from each other by numerous vesicles resulting in the loss of the typical Golgi structure (Figure 2D.b–c, arrows). Some of these vesicles present in the *sv*/*sv* spermatids were highly enlarged (Figure 2D.b–c, arrowheads) and we observed multiple proacrosomal vesicles (Figure 2D.d, white arrows), some of which were located at a distance from the upper pole of nucleus (Figure 2D.d, black arrow). Another structural disruption was identified in MYO6-deficient spermatids at the Golgi stage, where the acrosomal granules were not docked symmetrically within the acrosome sacs. In control spermatid, the acrosomal granule was attached symmetrically to the inner acrosomal membrane at the middle of the acroplaxome (Figure 2D.e, star), whereas in *sv*/*sv* spermatids these granules were often mislocated (Figure 2D.f). This phenomenon was also observed during the next stage, the early acrosome/cap stage (Figure 2D.g, compare with Figure 2D.h, stars). Interestingly, at this later phase of acrosomogenesis the disturbed Golgi morphology was still visible in *sv*/*sv* spermatids (Figure 2D.g, compare with Figure 2D.h, arrows). Quantification of the percentage

of spermatids with ultrastructural disruptions of the Golgi complex revealed that in control mice 9.49 ± 3.61% of spermatids exhibited Golgi structural defects compared to 40.83 ± 2.91% in *sv/sv* mice, indicating a four-fold increase of these defects in mutant spermatids (Figure 2B.b; $P = 0.0003$; $n = 3$ individual experiments on a pair of *sv/+* and *sv/sv* littermates each).

Loss of MYO6 affects the acrosomal granule positioning

We next analyzed the ultrastructure of *sv/sv* spermatids during the later cap phase, when the acrosome starts to flatten and forms a cap-like structure containing the electron-dense acrosomal granule (Figure 3A.a). The most striking and prominent structural disruption at this stage was the altered position of the acrosomal granule within *sv/sv* developing cap. While in control spermatid the acrosomal granule was anchored at the middle of the acroplaxome (Figure 3A.a, star), in the absence of MYO6 this central localization was lost (Figure 3A.b). In addition, in some *sv/sv* spermatids the acrosomal granules were detached from the acroplaxomes (Figure 3A.c) and its electron-dense content was reduced (Figure 3A.d). We have also observed a few "empty" acrosome sacs without any acrosomal granules in *sv/sv* spermatids; this phenotype corresponded usually with significantly enlarged vesicles adjacent to the deformed acrosomes (Figure 3A.e). In the next developmental step, the flattened cap further spread over the spermatid nucleus and became attached anteriorly to the Sertoli cell through the newly formed apical ectoplasmic specialization (Figure 3A.f, asterisks). In this phase, the asymmetry of the acrosome was still clearly visible in *sv/sv* spermatids (Figure 3A.g–h; compare with Figure 3A.f and A.g, black arrows with a bar). Our quantification revealed that in control mice only 11.69 ± 2.23% of spermatids exhibited defects in the acrosomal structure compared to 56.26 ± 4.30% of MYO6-deficient spermatids, indicating almost five-fold increase of atypical acrosome phenotype in mutant spermatids (Figure 3B; $P < 0.0001$; $n = 3$ individual experiments on a pair of *sv/+* and *sv/sv* littermates each). In summary, the loss of MYO6 in developing mouse spermatids leads to structural disruptions of the Golgi complex and affects formation of the acrosome during spermiogenesis.

MYO6 together with its binding partner TOM1/L2 are localized at the Golgi complex and developing acrosome

Acrosome biogenesis involves the delivery of proacrosomal vesicles from either the Golgi complex or from late endosomes/lysosomes to the nascent acrosome [28]. We previously demonstrated that MYO6 localizes to the Golgi stacks during the acrosomogenesis in wild-type mouse spermatids [12]. Indeed, our present immunofluorescent analysis shows that MYO6 is associated with the Golgi complex including the *cis*-Golgi domain (Figure 4A.a–a') and the region corresponding to the *trans*-Golgi network (Figure 4A.a–a") in *sv/+* spermatids, whereas no signal was observed in *sv/sv* cells confirming the specificity of our MYO6 antibodies (Figure 4A.b–b"). This confirms our previous results (using immunogold technique) showing that MYO6 localized to both Golgi sub-domains in wild-type mice males [12]. Targeting of MYO6 to different cellular compartments in mammalian cells involves a range of binding partners [15] and so we next analyzed which adaptor protein may function with MYO6 during acrosome biogenesis. We tested several MYO6 interacting proteins including TOM1/L2, GIPC1, optineurin, DOCK7, LRCH3, and LARG for their localization, and only observed the presence of TOM1/L2 in close vicinity to the Golgi complex. As demonstrated in Figure 4, TOM1/L2 that interacts with MYO6 in the endocytic pathway is present on vesicular-like structures localized between the spermatid nucleus and the Golgi complex labeled with anti-GM130 antibody, both in the control and *sv/sv* spermatids (Figure 4B.a–d).These results indicate that both MYO6 and its partner TOM1/L2 are present at/around the Golgi complex, although in different compartments. While MYO6 is associated with both *cis*-Golgi and *trans*-Golgi sub-domains, TOM1/L2 is present in a post-Golgi region that can either correspond to the *trans*-Golgi network or an endocytic compartment.

We next determined the localization of MYO6, TOM1/L2, and F-actin during the later acrosome phase, when the absence of MYO6 in *sv/sv* spermatids caused abnormal positioning of the acrosomal granule within the acrosome sac (Figures 2 and 3). First, we assessed the localization of MYO6 in control spermatids, where we observed a strong signal for MYO6 in the middle of the acroplaxome plate labeled for F-actin with the fluorochrome-conjugated phalloidin (Figure 5A.a, arrow) and a diffuse signal in the cytoplasm (Figure 5A). The area of MYO6 localization increased when the acrosome flattened and spread over the spermatid nucleus with a strong signal along the acroplaxome (Figure 5A.b–c, arrows). Visualizing the acrosome *en face* toward the microscope camera showed a strong concentration of MYO6 in the center of the actin-rich acroplaxome (Figure 5A.d). We next determined the localization of TOM1/L2 and found that it was present in the center of the acroplaxome (Figure 5B, arrows) in the same region of the acroplaxome plate that was also positive for MYO6 (compare Figure 5B.a–d and A.a–d). Moreover, although TOM1/L2 was detectable in spermatids dissected from the *sv/sv* male mice (Figure 5C.a–d), it was clearly mislocalized in the acroplaxome plate of the MYO6-deficient spermatids (compare Figure 5C.a–c and B.a–c, arrows).

TOM1/L2 contains a central GAT domain that binds ubiquitin that enables interaction of TOM1/L2 with ubiquitinylated proteins [29]. Indeed, we identified a strong signal for ubiquitin in the area corresponding to the acrosomal sac both in the control and mutant spermatids (Figure 5D). Interestingly, as observed for TOM1/L2, the ubiquitin-positive acrosomal granule was asymmetrically docked in the acroplaxome plate in *sv/sv* spermatids (Figure 5D.b). These results suggest that TOM1/L2 binds to ubiquitinylated proteins present in the membrane of the acrosomal granule to tether the granule via MYO6 to actin filaments in the acroplaxome plate, thereby anchoring the acrosomal granule in a central position within the sac (see Figure 8).

Next, we investigated the actin organization at the acroplaxome by staining actin filaments using fluorescent phalloidin. No obvious changes were observed in the F-actin network organization overlying the upper part of the spermatid nucleus beneath the acrosome in both control and mutant spermatids (Figure 5D.c–d). Staining of actin filaments, however, allowed us to detect position of the acrosomal granule attachment within the sac as a less actin-dense area (Figure 5D.c–d, arrows) and to visualize the acrosome asymmetry in *sv/sv* spermatids. Quantification of this abnormal phenotype indicated an almost four-fold increase of acrosome asymmetry in *sv/sv* spermatids in comparison to the control spermatids (6.47 ± 1.94% of asymmetric *sv/+* acrosomes in comparison to 24.62 ± 2.01% of *sv/sv* acrosomes; $P = 0.0004$; $n = 3$ individual experiments on a pair of *sv/+* and *sv/sv* littermates each) (Figure 5E). In summary, the loss of MYO6 in developing mouse spermatids leads to structural disruptions of the Golgi complex

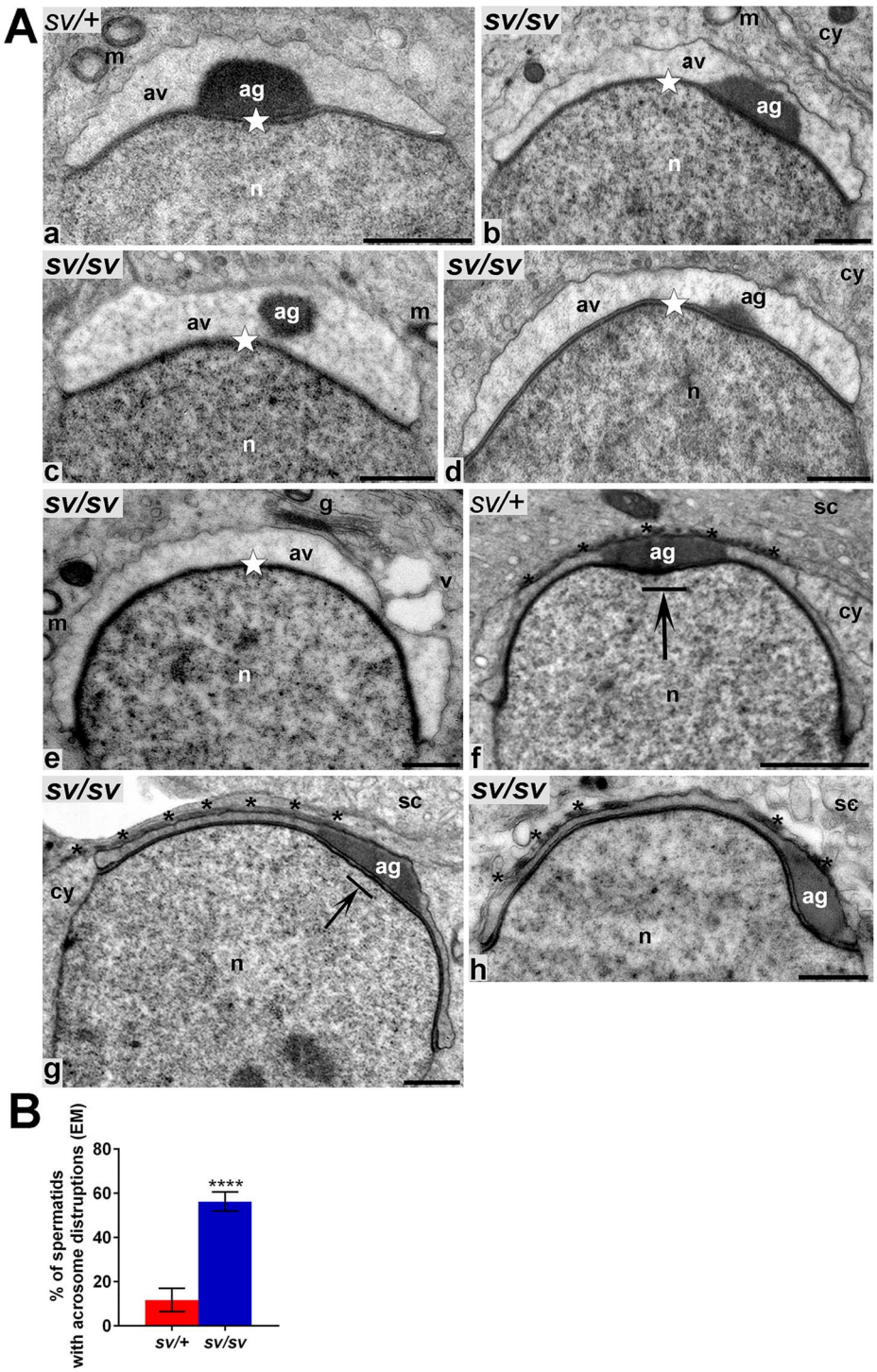

Figure 3. The acrosomogenesis in MYO6-deficient spermatids is altered (continued). (A) Ultrastructural analysis of *sv/+* and *sv/sv* spermatids during the consecutive phases of acrosomogenesis. ag, acrosomal granule; asterisks, apical ectoplasmic specialization; av, acrosomal vesicle; cy, cytoplasm; m, mitochondria; n, nucleus; and white star, acroplaxome. All other indications are explained in the text. Bars 1 μm. (B) The graphs depicting the mean percentage of *sv/+* and *sv/sv* cells that displayed the acrosome defects visualized with ultrastructural (EM) analysis. Counts were performed on at least four ultrathin sections of seminiferous tubules from randomly chosen fragments of fixed testes from $n = 3$ independent experiments. Error bars indicate SD.**** $P \leq 0.0001$.

and affects formation and position of the acrosomal granule during spermiogenesis.

Finally, we examined the exact localization of TOM1/L2 at the ultrastructural level in the developing acrosome using immunogold labeling (Figure 6). Consistent with our previous immunofluorescence results, we observed gold particles representing TOM1/L2 localization below the acrosomal granule at the position of the acroplaxome in control spermatids (Figure 6.a–a',

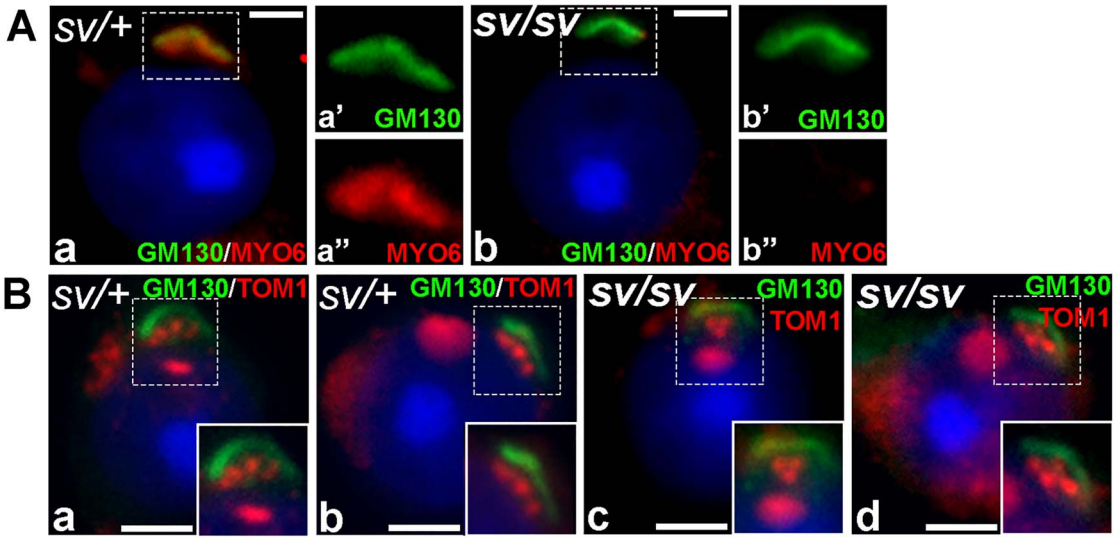

Figure 4. MYO6 and its binding partner TOM1/L2 are present at the Golgi complex. (A) Immunofluorescence localization of MYO6 (red) and GM130 (green) in *sv/+* and *sv/sv* round spermatids. Bars 2 μm. (B) Immunofluorescence localization of TOM1/L2 (TOM1 on images) (red) and GM130 (green) in *sv/+* and *sv/sv* round spermatids. Bars 2 μm.

arrowheads). In MYO6-depleted spermatids, we saw a similar pattern for TOM1/L2 localization at the acroplaxome, below the asymmetrically docked acrosomal granule (Figure 6.b–b'), indicating that in absence of MYO6, TOM1/L2 is still localized to this cellular compartment. These results suggest that MYO6 is one of the factors determining the correct positioning of this specific acrosomal sub-compartment.

The loss of MYO6 does not affect sperm function

To determine whether loss of MYO6 expression in mouse testes affects reproductive functions, we first assessed the overall morphology of 3-month-old mouse testes, which showed that testes dissected from *sv/sv* males were slightly smaller compared to the control organs (Figure 7A). Indeed, the average weight of heterozygous gonads was 102.50 ± 2.67 mg [sample size (*n*) = 8] while for homozygous mice this value was 91.13 ± 5.36 mg [sample size (*n*) = 8]. Thus, the weight of *sv/sv* testes was reduced by 11.09% ($P < 0.0001$) compared to the control organs (Figure 7B). However, testis to body weight ratio of *sv/sv* males was significantly larger than in control mice (*sv/+* = 0.38 ± 0.01, *sv/sv* = 0.47 ± 0.05; $P = 0.0175$; $n = 4$ pairs of *sv/+* and *sv/sv* littermates), reflecting the difference in body weight between control and mutant males (Figure 7C). It should be noted that *sv/sv* mice are smaller and they have less body fat compared to control mice.

Next, we determined whether structural defects observed in the mutant developing spermatids impact on the sperm production and evaluated the number of sperm collected from the caudae epididymides of 3-month-old *sv/+* and *sv/sv* littermates (Figure 7D). The production of total sperm and the sperm count was reduced by 14.19% in the *sv/sv* males compared to the control mice [*sv/+* = (1.55 ± 0.19) × 10^7, sample size (*n*) = 14; *sv/sv* = (1.33 ± 0.26) × 10^7, sample size (*n*) = 12; $P = 0.0173$]. We then analyzed the sperm head and acrosome structure of *sv/sv* mice using Hoechst and lectin PNA conjugate staining. Although we observed several spermatozoa with evident morphological defects in the head/acrosome shapes (Figure 7E), our analysis did not reveal any significant differences between mutant and control epididymal sperm [Figure 7F; *sv/+* = 3.00 ± 0.50% and *sv/sv* = 2.83 ± 0.76% of sperm with head/acrosome malformations; $P = 0.7676$; $n = 3$ individual experiments on a pair of *sv/+* and *sv/sv* littermates each]. To test the acrosome function of the *sv/sv* spermatozoa in vitro, we quantified the spontaneous acrosome reaction. We then treated the sperm with the calcium ionophore A23187 which triggers the acrosome reaction by increasing Ca^{2+} concentration in the sperm head (Figure 7G and H) and provides information about the potential sperm fertilizing ability. Incubation in capacitation medium caused a similar spontaneous acrosome reaction in epididymal sperm from control and mutant mice (Figure 7H; *sv/+* = 36.80 ± 4.91%, *sv/sv* = 38.33 ± 5.45%; $P = 0.6922$; $n = 4$ individual experiments on a pair of *sv/+* and *sv/sv* littermates each) and also after exposure to the calcium ionophore A23187 no significant changes between control and mutant mice were observed (Figure 7H; *sv/+* = 87.18 ± 5.46%, *sv/sv* = 85.85 ± 7.66%; $P = 0.7876$; $n = 4$ individual experiments on a pair of *sv/+* and *sv/sv* littermates each). Therefore, although the number of epididymal spermatozoa in MYO6-deficient mice was significantly reduced, their ability to perform the acrosomal reaction was not impaired.

Discussion

We have previously shown [12] that MYO6 is present in several actin-containing structures involved in mouse spermiogenesis, including the Golgi complex and the acrosome–acroplaxome complex (summarized in Figure 1). Here, we now demonstrate that this unique motor protein is involved in maintaining the structural integrity of these testis-specific structures that are crucial during the acrosome biogenesis in mouse.

Loss of MYO6 disrupts organization of the Golgi complex during acrosomogenesis

The actin cytoskeleton is required for the organization and function of the Golgi complex and depolymerization of actin filaments alters Golgi morphology and leads to dilation or fragmentation of its cisternae and to changes in the number of Golgi-derived

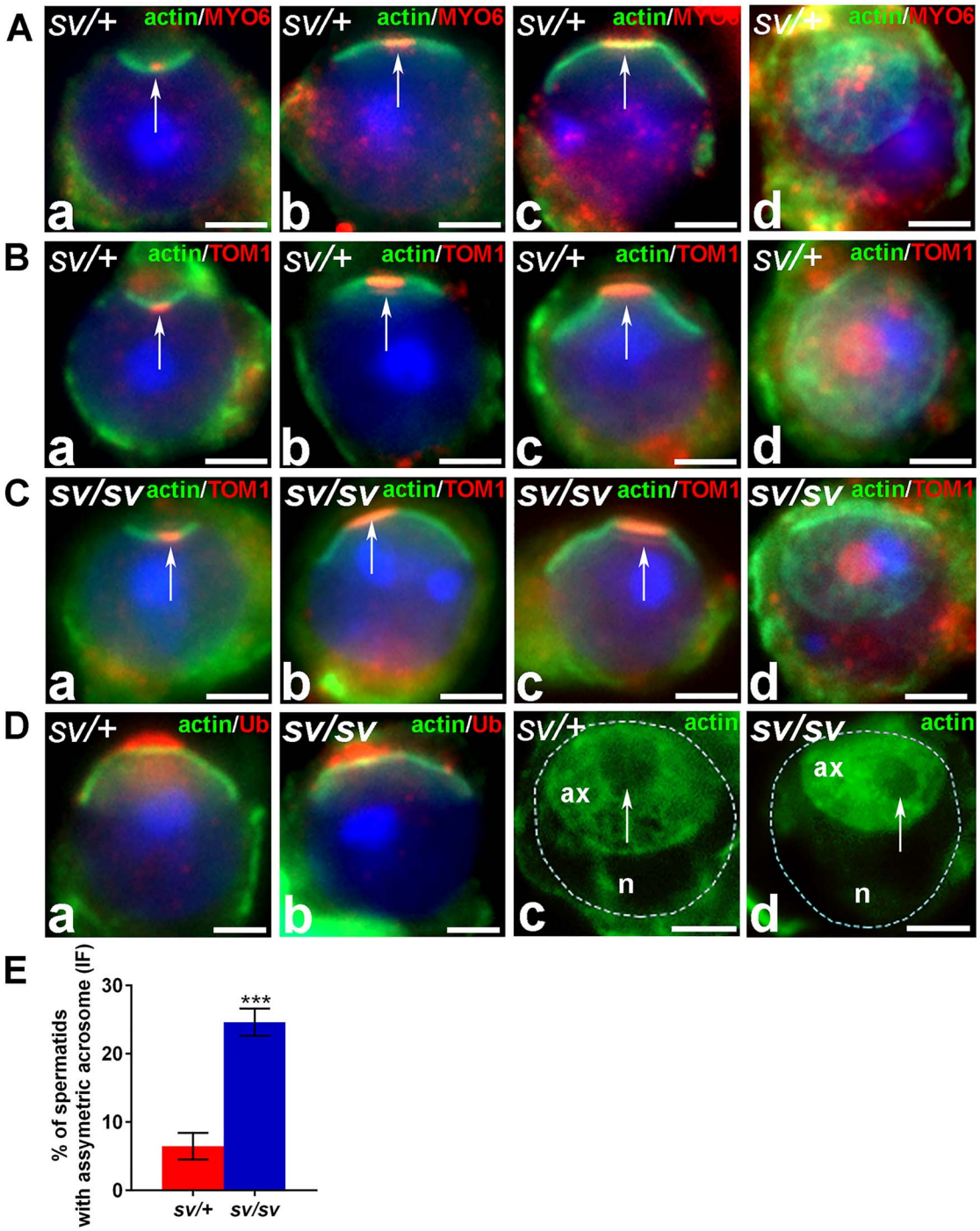

Figure 5. MYO6 with its binding partner TOM1/L2 maintains the proper localization the acrosomal granule. (A) Immunofluorescence localization of MYO6 (red) and actin (green) in *sv*/+ spermatids during the consecutive phases of spermiogenesis. Bars 2 μm. (B) Immunofluorescence localization of TOM1/L2 (TOM1 on images) (red) and actin (green) in *sv*/+ spermatids during consecutive phases of spermiogenesis. Bars 2 μm. (C) Immunofluorescence localization of TOM1/L2 (TOM1 on images) (red) and actin (green) in *sv/sv* spermatids during consecutive phases of spermiogenesis. Bars 2 μm. (D) Immunofluorescence localization of ubiquitin (red) and actin (green) in *sv*/+ and *sv/sv* spermatids (a–b); and fluorescence visualization of the actin-rich acroplaxome (ax, green) in *sv*/+ and *sv/sv* spermatids (c–d, white arrows showing the acrosomal granule docking site). Bars 2 μm. (E) The graph depicting the mean percentage of cells that displayed eccentric docking of the acrosomal granule. Counts were performed on >50 cells from $n = 3$ independent experiments. Error bars indicate SD. $^{***}P < 0.001$.

vesicles [30–32]. Several myosin motor proteins including MYO6 have been linked the Golgi complex and depletion of MYO6 causes changes in size of the Golgi complex and reductions in post-Golgi membrane trafficking in several cell types [22, 33–35]. Our recent ultrastructural study revealed that in wild-type mouse spermatids MYO6 is present throughout the Golgi stack from the *cis*- to the *trans*-side [12]. Here, we now show significant defects in Golgi organization in MYO6-depleted spermatids, including disorganized and incorrectly oriented Golgi complexes with separated stacks, swollen cisternae, and atypical accumulation

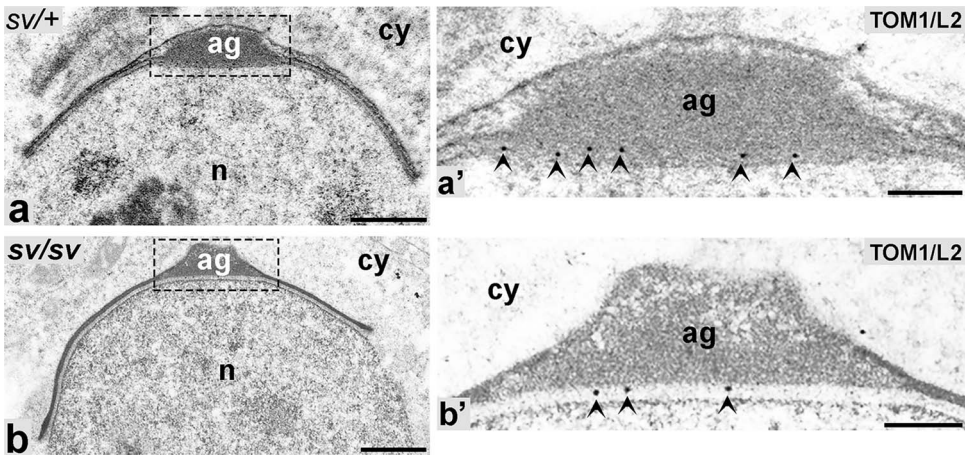

Figure 6. TOM1/L2 localizes to acroplaxome underneath the acrosomal granule in maturing spermatids. ag, acrosomal granule; cy, cytoplasm; and n, nucleus. Bars 1 μm (**a**–**b**), 250 nm (a'–b').

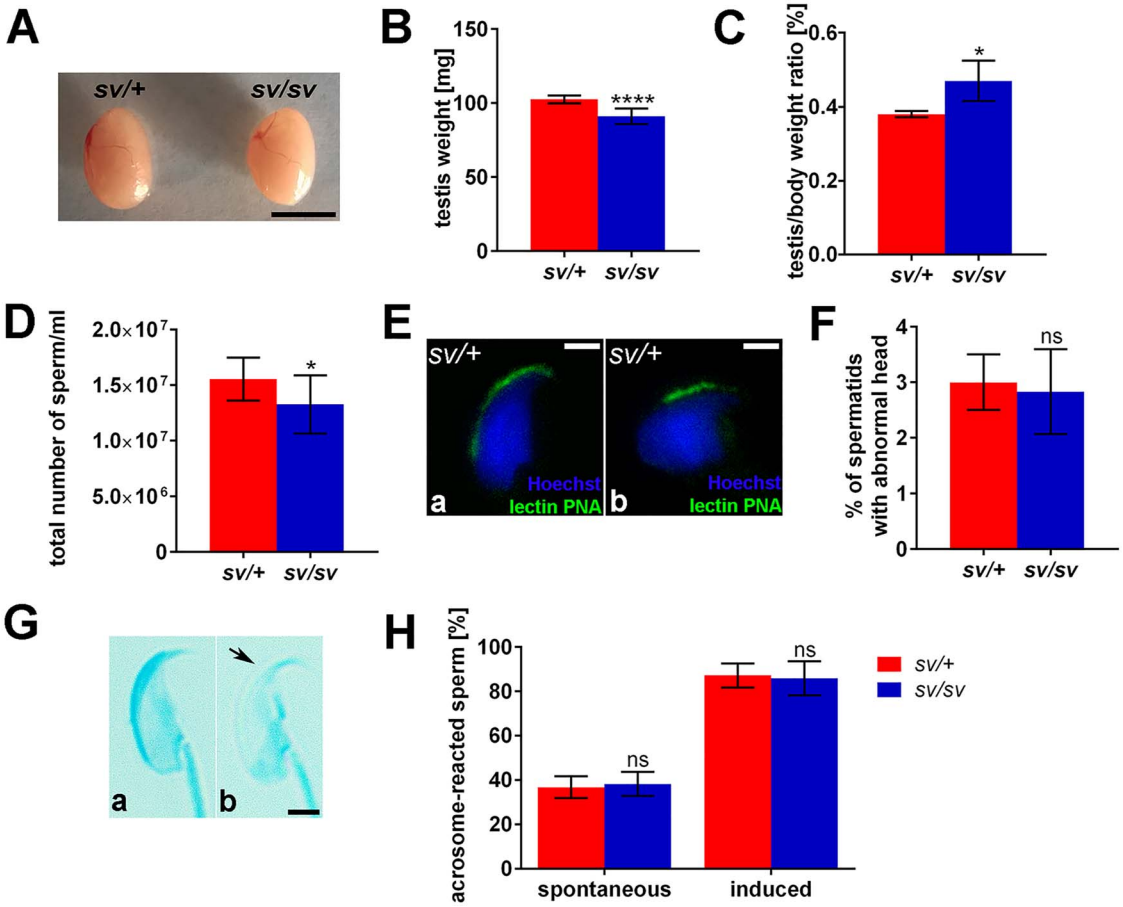

Figure 7. The loss of MYO6 results in the testis-associated phenotypic changes in Snell's waltzer males. (A) Image showing freshly isolated testis from *sv/+* and *sv/sv* males. Bar 0.5 cm. (B) Graph depicting the mean weight of *sv/+* ($n = 8$) and *sv/sv* ($n = 8$) testis. Error bars indicate SD. $^{****}P \leq 0.0001$. (C) Graph depicting the mean testis to body weight ratio of *sv/+* ($n = 4$) and *sv/sv* ($n = 4$) males. Error bars indicate SD. $^{*}P \leq 0.05$. (D) Graph depicting the mean total number of sperm isolated from *sv/+* ($n = 14$) and *sv/sv* ($n = 12$) caudae epididymides. Error bars indicate SD. $^{*}P \leq 0.05$. (E) Fluorescence images showing normally (a) and abnormally (b) shaped sperm heads stained with Hoechst and lectin PNA conjugate. Bar 2 μm. (F) Graph depicting the mean percentage of sperm with head/acrosome malformation isolated from caudae epididymides of *sv/+* ($n = 3$) and *sv/sv* ($n = 3$) males. Counts were performed on 200 sperm. Error bars indicate SD. ns, non-significant difference. (G) Light microscope images showing the head of unreacted (a) and acrosome-reacted (b) *sv/+* sperm. Black arrow shows the lack of acrosome staining after the acrosome reaction. Bar 2 μm. (H) The graph depicting the mean number of *sv/+* and *sv/sv* acrosome-reacted sperm after a spontaneous and ionophore-induced acrosomal reaction. Counts were performed on >150 sperm from $n = 4$ independent experiments. Error bars indicate SD. ns, non-significant difference.

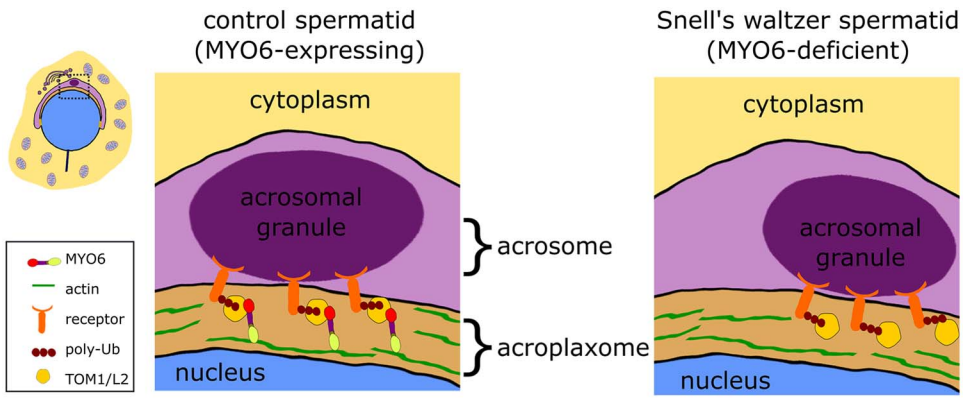

Figure 8. The model of MYO6-TOM1/L2 function in the acrosome formation. In the acroplaxome, below the acrosomal membrane, MYO6 binds with its motor domain to the actin filaments and with its tail to TOM1/L2. TOM1/L2 interacts via GAT domain with ubiquitinated transmembrane receptors docking the acrosomal granule in the center of the acrosome. In the absence of MYO6, the acrosomal granule is docked asymmetrical due to the displacement of TOM1/L2.

of vesicles between the separated cisternae. We therefore propose a structural role for MYO6 in linking the Golgi membranes to the surrounding actin filaments important for maintenance of Golgi stack orientation and morphology. These changes in Golgi integrity and morphology may also impair post-Golgi trafficking events linked to acrosome formation during acrosomogenesis that involves two distinct trafficking pathways—the anterograde pathway from the *trans*-Golgi network and the retrograde route via the endocytic pathway [28].

In mouse testes, the MYO6-small- and no-insert splice variants are expressed [12], which have been shown to play a role in cargo sorting and vesicle tethering and/or trafficking through the actin-rich regions in eukaryotic cells [36–39]. However, there is little evidence that MYO6 similar to myosin Va is involved in transporting proacrosomal granules along the actin filaments [10, 11]. We, therefore, propose that loss of Golgi morphology, the separation of the Golgi saccules, and the swelling of the Golgi cisternae observed in MYO6-deficient mouse spermatids support an anchoring role for MYO6 in the structural organization of the Golgi complex during acrosome biogenesis. In this model, actin assembly regulated by MYO6 and probably other ABPs provides the structural support that maintains Golgi morphology. Loss of MYO6 disturbs Golgi integrity, which may impact on the formation and transport of cargoes in the secretory pathway to the nascent acrosome–acroplaxome complex.

MYO6 together with TOM1/L2 maintains the symmetry of developing acrosome

Despite its importance in the fertilization process, very little is known about the molecular basis of acrosome development, how the acrosome is attached to the nuclear envelope, and how the acrosomal granule is kept in its correct position. There are only a few mouse mutants that show changes in the ectopic localization of the acrosomal granule similarly to *sv/sv* mice: these are *Zpbp1−/−* (zona pellucida binding protein 1), *Dpy19l2−/−* (testis-specific member of an uncharacterized gene family), *Acrbp−/−* (acrosin-binding protein), and *Pcsk4−/−* (protein convertase subtilisin/kexin type 4) [40–43]. In these mutants, the asymmetric localization of the acrosomal granule may be caused by destabilization of the multi-layered structure of the descending acrosome or the defective assembly/compaction of the acrosomal matrix proteins. However, in contrast to these mutants that show a more severe acrosome malformation, the observed dysfunction in the *sv/sv* developing acrosome is restricted to the asymmetric localization of the granule. The acrosome–acroplaxome complex contains actin filaments and actin-based molecular motors [3, 10], including MYO6 as previously shown [12]. Our present results suggest that MYO6 maintains the central position of the acrosome/acrosomal granule by anchoring this organelle to the spermatid nucleus. This hypothesis is consistent with the role of MYO6 in tethering of membranes to cortical actin filaments during the development of the intestinal brush border cells and the cochlear hair cells in the mouse inner ear [44, 45]. We also observed an elevated number of proacrosmal vesicles in *sv/sv* spermatids. A similar defect affecting the fusion of proacrosomal vesicles with the acrosome was observed in *TNAP-Atg7−/−* mice, in which ATG7 was selectively inactivated in germ cells [46]. The enzyme ATG7 lipidates the protein LC3 and the membrane-associated LC3 is required for autophagosome–lysosome fusion in the autophagy pathway. The acrosome is a lysosome-related organelle and so the authors postulated that in a similar way loss of ATG7 activity may cause defects in fusion of proacrosomal vesicles with the acrosome. Thus, since loss of MYO6 has also been shown to lead to an accumulation of autophagosomes due to a defect in autophagosome–lysosome fusion, the similar phenotypes in the MYO6 and ATG7-KO may both be linked to a function in the autophagy pathway [47].

Our results further show that not only MYO6 but also TOM1/L2 is present in the developing acrosome–acroplaxome complex in mouse. The exact cellular function/s of this endocytic MYO6 adaptor protein in mammals are less well understood; however, the MYO6-TOM1/L2 complex is likely to play a role in endocytic cargo sorting and has been shown to facilitate the maturation of autophagosomes enabling their fusion with the lysosome [47]. In addition, MYO6 facilitates the tethering of early endosomes to cortical microfilaments important for maturation of nascent endosomes and downstream signaling events, which precedes the cargo processing in the early endosomes [48]. Taken together these findings support an anchoring role of MYO6 during the acrosome formation in mouse. A hypothetical model of MYO6 action at the acrosome–acroplaxome complex is summarized in Figure 8 .

Conclusions

The ultrastructural disruptions observed in MYO6-deficient spermatids in Snell's waltzer mice suggests that in mammals, similar to invertebrates, MYO6 plays an anchoring role during the key events

of spermiogenesis by either organizing the actin cytoskeleton or by tethering of different cargo/membranes to testis-specific actin structures. Other myosin motors, such as Va and VIIa, are also required in mammalian spermiogenesis for membrane trafficking events during acrosomogenesis and spermatid adhesion to the Sertoli cell [10, 11, 49–51]. In contrast to Snell's waltzer males, however, myosin VIIa-deficient rat males show premature release of spermatids and numerous defects in spermatozoa [51]. Although no morphological defects were observed in *sv/sv* sperm, it is possible that spermatids with abnormally formed acrosomes, as we observed in *sv/sv* mice, are phagocytozed by Sertoli cells. This may explain the slightly reduced number of sperm (this work) and lower fertility of *sv/sv* males (our previous work [26]). Taken together our findings suggest that the actin cytoskeleton, a number of different ABPs, and several myosin motor proteins including MYO6 play highly specialized sequential roles during the complex process of spermiogenesis in mammals.

Supplementary data

Supplementary data are available at *BIOLRE* online.

Acknowledgments

We want to thank Dr Vira Chumak, Ms Małgorzata Topolewska, and Dr Liliia Lehka from the Laboratory of Molecular Basis of Cell Motility (Nencki Institute of Experimental Biology, Polish Academy of Sciences, Warsaw, Poland) for their invaluable help with animals and tissue harvesting and Dr Christopher Batters from the Cambridge Institute for Medical Research (University of Cambridge, Cambridge, UK) for critical reading of the manuscript.

Conflicts of Interest

The authors declare that no competing interests exist.

Author Contributions

P.Z., M.L., and F.B. conceived and designed the experiments. P.Z. performed the experiments. P.Z., M.L., F.B., and M.J.R. analyzed the data. P.Z., M.L., and F.B. wrote the paper.

References

1. Dunleavy JEM, O'Bryan MK, Stanton PG, O'Donnell L. The cytoskeleton in spermatogenesis. *Reproduction* 2019; **157**:53–72.
2. Elkis Y, Bel S, Rahimi R, Lerer-Goldstein T, Levin-Zaidman S, Babushkin T, Shpungin S, Nir U. TMF/ARA160 governs the dynamic spatial orientation of the Golgi apparatus during sperm development. *PLoS One* 2015; **10**:e014277.
3. Kierszenbaum AL, Rivkin E, Tres LL. Acroplaxome, an F-actin-containing plate, anchors the acrosome to the nucleus during shaping of the spermatid head. *Mol Biol Cell* 2003; **14**:4628–4640.
4. Wei YL, Yang WX. The acroframosome-acroplaxome-manchette axis may function in sperm head shaping and male fertility. *Gene* 2018; **660**:28–40.
5. Upadhyay RD, Kumar AV, Ganeshan M, Balasinor NH. Tubulobulbar complex: cytoskeletal remodeling to release spermatozoa. *Reprod Biol Endocrin* 2012; **10**:27–34.
6. Wen Q, Mruk D, Tang EI, Wong CKC, Lui W, Lee WM, Xiao X, Silvestrini B, Cheng CY. Cell polarity and cytoskeletons – lesson from the testis. *Semin Cell Dev Biol* 2018; **81**:21–32.
7. Russell LD. Cytochalasin D causes focal lifting of the acrosome from the spermatid nucleus during spermiogenesis of the rat. *Anat Rec* 1989; **223**:A99.
8. Kierszenbaum AL, Rivkin E, Tres LL. Expression of Fer testis (FerT) tyrosine kinase transcript variants and distribution site of FerT during the development of the acrosome-acroplaxome-manchette complex in rat spermatids. *Dev Dyn* 2008; **237**:3882–3891.
9. Behnen M, Murk K, Kursula P, Cappallo-Obermann H, Rothkegel M, Kirszenbaum AL, Kirchhoff C. Testis-expressed profilins 3 and 4 show distinct functional characteristics and localize in the acroplaxome–manchette complex in spermatids. *BMC Cell Biol* 2009; **10**:34.
10. Kierszenbaum AL, Rivkin E, Tres LL. The actin-based motor myosin Va is a component of the acroplaxome, an acrosome-nuclear-envelope junctional plate, and of manchette-associated vesicles. *Cytogenet Genome Res* 2003; **103**:337–344.
11. Hayasaka S, Terada Y, Suzuki K, Murakawa H, Tachibana I, Sankai T, Murakami T, Yaegashi N, Okamura K. Intramanchette transport during primate spermiogenesis: expression of dynein, myosin Va, motor recruiter myosin Va, VIIa-Rab27a/b interacting protein, and Rab27b in the manchette during human and monkey spermiogenesis. *Asian J Androl* 2008; **10**:561–568.
12. Zakrzewski P, Lenartowski R, Rędowicz MJ, Miller KG, Lenartowska M. Expression and localization of myosin VI in developing mouse spermatids. *Histochem Cell Biol* 2017; **148**:445–462.
13. Roberts R, Lister I, Schmitz S, Walker M, Veigel C, Trinick J, Buss F, Kendrick-Jones J. Myosin VI: cellular functions and motor properties. *Philos Trans R Soc Lond B Biol Sci* 2004; **359**:1931–1944.
14. Tumbarello DA, Kendrick-Jones J, Buss F. Myosin VI and its cargo adaptors - linking endocytosis and autophagy. *J Cell Sci* 2013; **126**: 2561–2570.
15. de Jonge JJ, Batters C, O'Loughlin T, Arden SD, Buss F. The MYO6 interactome: selective motor-cargo complexes for diverse cellular processes. *FEBS Lett* 2019; **593**:1494–1507.
16. Mermall V, Miller KG. The 95F unconventional myosin is required for proper organization of the *Drosophila* syncytial blastoderm. *J Cell Biol* 1995; **129**:1575–1588.
17. Deng W, Leaper K, Bownes M. A targeted gene silencing technique shows that *Drosophila* myosin VI is required for egg chamber and imaginal disc morphogenesis. *J Cell Sci* 1999; **112**:3677–3690.
18. Millo H, Leaper K, Lazou V, Bownes M. Myosin VI plays a role in cell-cell adhesion during epithelial morphogenesis. *Mech Dev* 2004; **121**:1335–1351.
19. Noguchi T, Lenartowska M, Miller KG. Myosin VI stabilizes an actin network during *Drosophila* spermatid individualization. *Mol Biol Cell* 2006; **17**:2559–2571.
20. Isaji M, Lenartowska M, Noguchi T, Frank DJ, Miller KG. Myosin VI regulates actin structure specialization through conserved cargo-binding domain sites. *PLoS One* 2011; **6**:e22755.
21. Avraham KB, Hasson T, Steel KP, Kingsley DM, Russell LB, Mooseker MS, Copeland NG, Jenkins NA. The mouse *Snell's waltzer* deafness gene encodes an unconventional myosin required for structural integrity of inner ear hair cells. *Nat Genet* 1995; **11**:369–375.
22. Warner CL, Stewart A, Luzio JP, Steel KP, Libby RT, Kendrick-Jones J, Buss F. Loss of myosin VI reduces secretion and the size of the Golgi in fibroblasts from *Snell's waltzer* mice. *EMBO J* 2003; **22**: 569–579.
23. Osterweil E, Wells DG, Mooseker MS. A role for myosin VI in postsynaptic structure and glutamate receptor endocytosis. *J Cell Biol* 2005; **168**:329–338.
24. Puri C. Loss of myosin VI no insert isoform (NoI) induces a defect in clathrin-mediated endocytosis and leads to caveolar endocytosis of transferrin receptor. *J Biol Chem* 2009; **284**:34998–35014.
25. Schubert T, Gleiser C, Heiduschka P, Franz C, Nagel-Wolfrum K, Sahaboglu A, Weisschuh N, Eske G, Rohbock K, Rieger N, Paquet-Durand F, Wissinger B et al. Deletion of myosin VI causes slow retinal optic neuropathy and age-related macular degeneration (AMD)-relevant retinal phenotype. *Cell Mol Life Sci* 2015; **72**:3953–3969.

26. Zakrzewski P, Suwińska A, Lenartowski R, Rędowicz MJ, Buss F, Lenartowska M. Myosin VI maintains the actin-dependent organization of the tubulobulbar complexes required for endocytosis during mouse spermiogenesis. *Biol Reprod* 2020; **102**:863–875.
27. Young JS, Guttman JA, Vaid KS, Shahinian H, Vogl AW. Cortactin (CTTN), N-WASP (WASL), and clathrin (CLTC) are present at podosome-like tubulobulbar complexes in the rat testis. *Biol Reprod* 2009; **80**:153–161.
28. Berruti G, Paiardi C. Acrosome biogenesis: revisiting old questions to yield new insights. *Spermatogenesis* 2011; **1**:95–98.
29. Yamakami M, Yoshimori T, Yokosawa H. Tom1, a VHS domain-containing protein, interacts with tollip, ubiquitin, and clathrin. *J Biol Chem* 2003; **278**:52865–52872.
30. Egea G, Serra-Peinado C, Salcedo-Sicilia L, Gutiérrez-Martínez E. Actin acting at the Golgi. *Histochem Cell Biol* 2013; **140**:347–360.
31. Gurel PS, Hatch AL, Higgs HN. Connecting the cytoskeleton to the endoplasmic reticulum and Golgi. *Curr Biol* 2014; **24**:R660–R672.
32. Kulkarni-Gosavi P, Makhoul C, Gleeson PA. Form and function of the Golgi apparatus: scaffolds, cytoskeleton and signaling. *FEBS Lett* 2019; **593**:2289–2305.
33. Sahlender DA, Roberts RC, Arden SD, Spudich G, Taylor MJ, Luzio JP, Kendrick-Jones J, Buss F. Optineurin links myosin VI to the Golgi complex and is involved in Golgi organization and exocytosis. *J Cell Biol* 2005; **169**:285–295.
34. Majewski Ł, Sobczak M, Wasik A, Skowronek K, Rędowicz MJ. Myosin VI in PC12 cells plays important roles in cell migration and proliferation but not in catecholamine secretion. *J Muscle Res Cell Motil* 2011; **32**:291–302.
35. Karolczak J, Pavlyk I, Majewski Ł, Sobczak M, Niewiadomski P, Rzhepetskyy Y, Sikorska A, Nowak N, Pomorski P, Prószyński T, Ehler E, Rędowicz MJ. Involvement of unconventional myosin VI in myoblast function and myotube formation. *Histochem Cell Biol* 2015; **144**:21–38.
36. Buss F, Arden SD, Lindsay M, Luzio JP, Kendrick-Jones J. Myosin VI isoform localized to clathrin-coated vesicles with a role in clathrin-mediated endocytosis. *EMBO J* 2001; **20**:3676–3684.
37. Au JS, Puri C, Ihrke G, Kendrick-Jones J, Buss F. Myosin VI is required for sorting of AP-1B-dependent cargo to the basolateral domain in polarized MDCK cells. *J Cell Biol* 2007; **177**:103–114.
38. Tomatis VM, Papadopulos A, Malintan NT, Martin S, Wallis T, Gormal RS, Kendrick-Jones J, Buss F, Meunier FA. Myosin VI small insert isoform maintains exocytosis by tethering secretory granules to the cortical actin. *J Cell Biol* 2013; **200**:301–320.
39. Bond LM, Peden AA, Kendrick-Jones J, Sellers JR, Buss F. Myosin VI and its binding partner optineurin are involved in secretory vesicle fusion at the plasma membrane. *Mol Biol Cell* 2011; **22**:54–65.
40. Lin YN, Roy A, Yan W, Burns KH, Matzuk MM. Loss of zona pellucida binding proteins in the acrosomal matrix disrupts acrosome biogenesis and sperm morphogenesis. *Mol Cell Biol* 2007; **2**:6794–6805.
41. Pierre V, Martinez G, Coutton C, Delaroche J, Yassine S, Novella C, Pernet-Gallay K, Hennebicq S, Ray PF, Arnoult C, Pierre V, Martinez G et al. Absence of Dpy19l2, a new inner nuclear membrane protein, causes globozoospermia in mice by preventing the anchoring of the acrosome to the nucleus. *Development* 2012; **139**:2955–2965.
42. Tardif S, Guyonnet B, Cormier N, Cornwall GA. Alteration in the processing of the ACRBP/sp32 protein and sperm head/acrosome malformations in proprotein convertase 4 (PCSK4) null mice. *Mol Hum Reprod* 2012; **18**:298–307.
43. Kanemori Y, Koga Y, Sudo M, Kang W, Kashiwabara S, Ikawa M, Hasuwa H, Nagashima K, Ishikawa Y, Ogonuki N, Ogura A, Baba T. Biogenesis of sperm acrosome is regulated by pre-mRNA alternative splicing of Acrbp in the mouse. *Proc Natl Acad Sci USA* 2016; **113**:e3696–e3705.
44. Hegan PS, Giral H, Levi M, Mooseker MS. Myosin VI is required for maintenance of brush border structure, composition, and membrane trafficking functions in the intestinal epithelial cell. *Cytoskeleton (Hoboken)* 2012; **69**:235–251.
45. Self T, Sobe T, Copeland NG, Jenkins NA, Avraham KB, Steel KP. Role of myosin VI in the differentiation of cochlear hair cells. *Dev Biol* 1999; **214**:331–341.
46. Wang H, Wan H, Li X, Liu W, Chen Q, Wang Y, Yang L, Tang H, Zhang X, Duan E, Zhao X, Gao F et al. Atg7 is required for acrosome biogenesis during spermatogenesis in mice. *Cell Res* 2014; **24**:852–869.
47. Tumbarello DA, Waxse BJ, Arden SD, Bright NA, Kendrick-Jones J, Buss F. Autophagy receptors link myosin VI to autophagosomes to mediate Tom1-dependent autophagosome maturation and fusion with the lysosome. *Nat Cell Biol* 2012; **14**:1024–1035.
48. Masters TA, Tumbarello DA, Chibalina MV, Buss F. MYO6 regulates spatial organization of signaling endosomes driving AKT activation and actin dynamics. *Cell Rep* 2017; **19**:2088–2210.
49. Wen Q, Tang EI, Xiao X, Gao Y, Chu DS, Mruk DD, Silvestrini B, Cheng CY. Transport of germ cells across the seminiferous epithelium during spermatogenesis - the involvement of both actin- and microtubule-based cytoskeletons. *Tissue Barriers* 2016; **4**:e1265042.
50. Velichkova M, Guttman J, Warren C, Eng L, Kline K, Vogl AW, Hasson T. A human homologue of *Drosophila* kelch associates with myosin-VIIa in specialized adhesion junctions. *Cell Motil Cytoskeleton* 2002; **51**:147–164.
51. Wen Q, Wu S, Lee WM, Wong CKC, Lui W, Silvestrini B, Cheng CY. Myosin VIIa supports spermatid/organelle transport and cell adhesion during spermatogenesis in the rat testis. *Endocrinology* 2019; **160**:484–503.
52. Buss F, Kendrick-Jones J, Lionne C, Knight AE, Côté GP, Paul LJ. The localization of myosin VI at the Golgi complex and leading edge of fibroblasts and its phosphorylation and recruitment into membrane ruffles of A431 cells after growth factor stimulation. *J Cell Biol* 1998; **143**:1535–1545.